Observation of temperature-dependent Fermi surface evolution at the valence transition of YbInCu₄

Hiroaki Anzai [1,*], Atsushi Hariki [1], Hitoshi Sato,[2] Masashi Arita,[2] Tao Zhuang,[3] and Koichi Hiraoka[3]

[1]*Graduate School of Engineering, Osaka Metropolitan University, Sakai 599-8531, Japan*

[2]*Hiroshima Synchrotron Radiation Center, Hiroshima University, Higashi-Hiroshima 739-0046, Japan*

[3]*Graduate School of Science and Engineering, Ehime University, Matsuyama 790-8577, Japan*

YbInCu₄, which is an excellent material for understanding first-order valence transitions, has been studied for over three decades. However, direct evidence for the evolution of the Fermi surface at the valence transition temperature T_V has not been obtained owing to the complicated nature of the electronic band structure near the Fermi level E_F. In this study, we use angle-resolved photoemission spectroscopy measurements and local density approximation calculations to reveal the temperature-dependent Fermi surface evolution in YbInCu₄. We experimentally identify the topology of the Fermi surface and find that the area of the Fermi surface increases with an accompanying decrease in the Fermi velocity below T_V. These observations demonstrate a reconstruction from a small to a large Fermi surface. Moreover, we theoretically reveal that the conduction bands of Cu s, p, and d and In s and p states hybridize with the f bands (c-f hybridization), thereby inducing a dramatic change in the band structure near E_F. Interestingly, a Van Hove singularity with the saddle point moves to E_F owing to c-f hybridization. We propose that the c-f hybridization and the enhancement in the density of states at E_F should be incorporated in the scenarios of the first-order valence transition of YbInCu₄.

I. INTRODUCTION

The first-order valence transition is one of the most controversial topics in Ce- and Yb-based compounds. Two nearly degenerate $4f$ valence configurations fluctuate by a small perturbation, such as temperature, pressure, and magnetic field [1,2]. Although the mean-valence value of rare-earth ions changes slowly in general, a handful of systems exhibit a sharp change in their values at low temperatures, namely, the first-order character of the valence transition. This unusual property is closely associated with Kondo coupling between the bandlike conduction electrons and the localized $4f$ spin moments, mediated by c-f hybridization and the f-f electron interaction [2]. Indeed, a relation of the first-order valence transition with crossover from the Kondo state to the mixed-valence state near the quantum critical point (QCP) has been discussed [3,4]. Because the f-f interaction strength does not significantly depend on the perturbation, the experimental challenge of the mechanism of the first-order valence transition lies in understanding the evolution of the c-f hybridization.

We focus on the first-order valence transition of the $4f^{13}$ (Yb³⁺) and $4f^{14}$ (Yb²⁺) configurations in YbInCu₄. The valence transition temperature is determined to be $T_V = 42$ K from a discontinuous jump in the magnetic susceptibility, specific heat, and electrical resistivity [5–8]. Mössbauer and x-ray absorption spectroscopy measurements revealed that the Yb valence changes from $z \simeq 2.9$ in the high-temperature phase to $z \simeq 2.8$ in the low-temperature phase [5,6]. This valence transition is suppressed by pressure or magnetic field,

indicating that YbInCu₄ is located in the vicinity of the QCP [8,9]. A notable feature is that the Kondo temperature T_K varies from ~ 25 K ($T > T_V$) to ~ 400 K ($T < T_V$) [8–10]. In the single-impurity Kondo or Anderson model description, T_K increases with the lifting of the degeneracy of the $4f$ states by a crystalline electric field (CEF) and anisotropy in the c-f hybridization [11]. Because the lattice volume change of 0.5% at T_V is small in YbInCu₄, the temperature dependence of the c-f hybridization is expected to play a dominant role in the dramatic change in T_K and possibly the emergence of the first-order valence transition [12–14].

The change in the electronic band structure near E_F serves as a direct measure of the c-f hybridization. The phase transitions, such as superconductivity and antiferromagnetism, usually occur with a change in the volume or area of the Fermi surface and are thus triggered by a Fermi surface instability [15,16]. For the $4f$-electron systems, the c-f hybridization forms heavy quasiparticle bands near E_F and causes reconstruction from a small to a large Fermi surface [17–19]. A recent high-resolution Compton scattering study on YbRh₂Si₂ revealed the temperature-driven Fermi surface reconstruction [20]. In the case of YbInCu₄, an increase in the hybridization strength is identified below T_V, but the shape and size of the Fermi surfaces remain unclear [21,22]. Another Fermi surface instability arises from a Van Hove singularity (VHS) at a saddle point of energy dispersion in momentum space [23]. When the Fermi energy is close to the VHS, instabilities could occur, leading to new phases with a change in the Fermi surface volume [24]. To pin down the driving factor for the valence transition in YbInCu₄, a thorough investigation of the momentum and temperature dependences of the electronic structure near E_F is required.

*anzai@omu.ac.jp

In this paper, we report angle-resolved photoemission spectroscopy (ARPES) measurements and a density functional theory calculation within the local density approximation (LDA) for YbInCu$_4$. We experimentally identify the shape of the Fermi surface in both the low- and high-temperature phases. The changes in the Fermi surface area and the Fermi velocity provide evidence of the development of the c-f hybridization below T_V, demonstrating the crossover from a small to a large Fermi surface. In particular, the saddle point Van Hove singularity and the CEF-split f bands cause a high density of states at E_F. We discuss possible mechanisms for the first-order valence transition of YbInCu$_4$.

II. METHODS

High-quality single crystals of YbInCu$_4$ were synthesized using the flux method [25,26]. ARPES measurements were performed at BL-9A of the Hiroshima Synchrotron Radiation Center (HSRC). The samples were cleaved *in situ* along the (111) crystal plane and kept under an ultrahigh vacuum (3.8×10^{-9} Pa) during the measurements. All data were taken using circularly polarized photons of synchrotron radiation. Photoemission spectra over a wide energy range were measured with a photon energy of $h\nu = 38$ eV. Other spectra were acquired with $h\nu = 24$ eV photons. The overall energy resolution was set to 17 meV. We note that the cleaved surface and the crystal orientation were better quality than those in our previous experimental results [22].

Density functional theory calculations were performed using the WIEN2K package [27] implementing the augmented plane wave and local orbital method. We use the LDA scheme for the exchange-correlation potential [28] and present a band structure as a guide to understand the overall dispersive features of the conduction electrons in the ARPES data. The LDA scheme suffers from inaccurate description of the $4f$ energy levels and electronic correlation effects, and thus, it gives a crude result for the $4f$ bands. More accurate treatment of electronic correlation using, for instance, the LDA plus dynamical mean-field theory (DMFT) scheme [29,30] is necessary to describe the $4f$ band energies and to trace the temperature evolution. However, the determination of computational parameters in the LDA+DMFT scheme such as the double-counting correction and electron-electron interaction parameter, which are often sensitive to the $4f$ energy levels, may require a detailed comparison with high-resolution photoemission data [31] beyond the present experimental instrument.

We thus employ an open-core approximation for the localized Yb $4f$ electrons in the LDA calculation [32]. The LDA result with the $4f$ electrons in the valence state is also shown below to infer a band structure change due to c-f hybridization, although the binding energies and spectral weights cannot be directly compared with the ARPES data since they can be strongly generalized by correlation effects. To visualize the element character of the dispersive bands and a possible c-f hybridization effect on a specific momentum in the Brillouin zone on the LDA level, we plot the band structure projected on the Wannier functions constructed from the LDA bands spanning Yb f, d, and p; Cu s, p, and d; and In s and p orbitals using the WIEN2WANNIER and WANNIER90
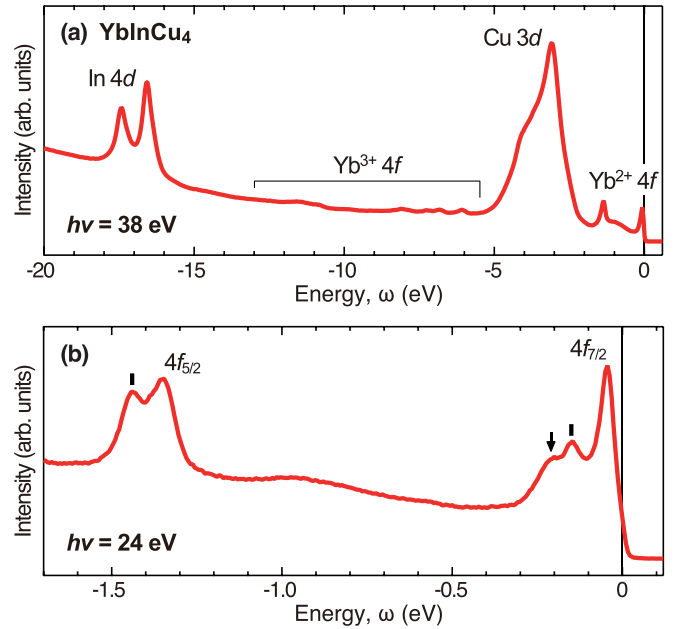

FIG. 1. Angle-integrated photoemission spectra of YbInCu$_4$ at $T = 10$ K in the low-temperature phase. (a) Photoemission spectra over a wide energy range taken with a photon energy of $h\nu = 38$ eV. (b) Valence-band photoemission spectra taken with $h\nu = 24$ eV photons. The vertical bars indicate the energy positions of Yb $4f$-derived electronic states. The arrow represents a characteristic structure discussed in the text.

packages [33,34]. The energy window in the Wannierization is set to [−10 eV, 20 eV], and 110 Wannier functions are constructed for the tight-binding model; details can be found in Ref. [31]. Then, the hopping elements between the Yb $4f$ and other Wannier orbitals in the tight-binding Hamiltonian are manually set to zero to simulate the electronic bands without the c-f hybridization. The experimental structure above T_V is adopted in the LDA calculation [35].

III. RESULTS AND DISCUSSION

Figure 1(a) shows the angle-integrated photoemission spectra of YbInCu$_4$ in a wide energy range taken at $T = 10$ K with a photon energy of $h\nu = 38$ eV. We observe a double peak at $|\omega| \simeq 16.5$ and 17.5 eV. These peaks are assigned to the spin-orbit splitting of the In $4d$ states, according to the tabulated values of the core-level binding energy [36]. The Yb^{3+} $4f$ states are observed at $5.5 < |\omega| < 13$ eV as multiplet structures due to the Coulomb interaction between two $4f$ holes in the photoelectron final states [37–40]. The large spectral weight at $|\omega| \sim 3$ eV is derived from the Cu $3d$ states and is well explained by the band structure calculation [41]. Two peaks near E_F are the spin-orbit split Yb^{2+} $4f$ states: the $4f_{7/2}$ and $4f_{5/2}$ states are located at $|\omega| \simeq 0.04$ and 1.35 eV, respectively [37–44].

In Fig. 1(b), we show the valence-band photoemission spectra taken with a photon energy of $h\nu = 24$ eV. The broad spectral weight at $|\omega| \simeq 1.0$ eV is assigned to the surface contribution of the divalent Yb ion at the topmost surface layer [37]. A small peak is observed at $|\omega| \simeq 0.13$ eV in
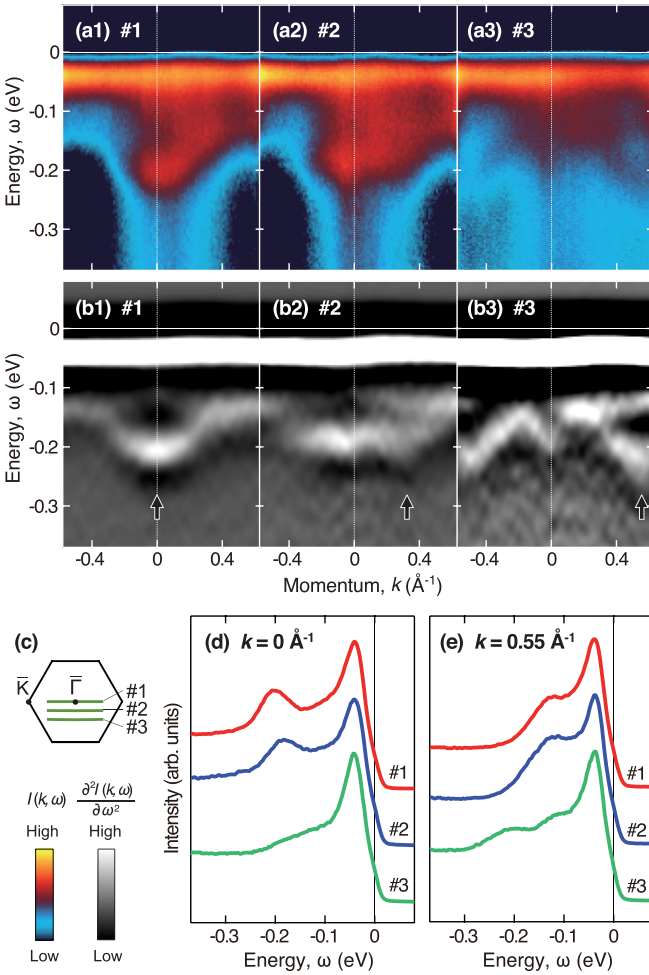
FIG. 2. ARPES spectra of YbInCu$_4$ measured at $T = 10$ K. (a1)–(a3) ARPES intensity plot $I(k, \omega)$ taken along three momentum cuts (#1–#3) of the two-dimensional surface Brillouin zone, marked by green lines in (c). (b1)–(b3) Second energy derivatives of the ARPES spectra $\partial^2 I(k, \omega)/\partial\omega^2$ for the data set in (a1)–(a3). The black arrows indicate a momentum variation of the band dispersion discussed in the text. (c) Schematic figure of the two-dimensional surface Brillouin zone for the (111) crystal plane of YbInCu$_4$. The thick green lines represent the locations of the momentum cuts for #1, #2, and #3. (d) Energy distribution curves at $k = 0$ Å^{-1} for the data in (a1)–(a3). (e) The same data set as in (d), but at $k = 0.55$ Å^{-1}.

the neighborhood of the $4f_{7/2}$ state, as marked by the vertical bar in Fig. 1(b). A similar peak appears on the high-energy side of the $4f_{5/2}$ state. The energy splitting between the $4f_{7/2}$ main peak and the small peak coincides with that of the spin-orbit partner of the $4f_{5/2}$ state, indicating that the peak at $|\omega| \simeq 0.13$ eV originates from the Yb $4f$ states. An additional shoulder is clearly observed at $|\omega| \simeq 0.21$ eV, as indicated by an arrow.

We performed ARPES measurements over a wide momentum region to understand the electronic band structure near E_F. Figures 2(a1)–2(a3) show the ARPES intensity plot $I(k, \omega)$ along three momentum cuts (#1–#3) of the surface-projected Brillouin zone in Fig. 2(c). The data were recorded at $T = 10$ K in the low-temperature phase. For a better understanding of the band dispersion, we also plot the second

derivative of the ARPES spectra with respect to the energy $\partial^2 I(k, \omega)/\partial\omega^2$ in Figs. 2(b1)–2(b3). The flat band of the $4f_{7/2}$ state is clearly seen at $|\omega| \simeq 0.04$ eV and corresponds to the sharp and intense peak near E_F, as observed in the energy-distribution curves (EDCs) in Figs. 2(d) and 2(e). The momentum dependence of the $4f_{7/2}$ band at 0.04 eV is negligible within the present experimental resolution.

The bands on the high-energy side of the $4f_{7/2}$ main peak have momentum dependence. As shown by the spectra along cut #1 in Figs. 2(a1) and 2(b1), the band at $|\omega| \simeq 0.13$ eV splits into upper and lower branches around $k \simeq 0$ Å^{-1} of the $\overline{\Gamma}$ point. From the peak position of the EDCs in Fig. 2(d), the bottom of the lower branch is estimated to be $|\omega| \simeq 0.21$ eV, corresponding to the energy of the small shoulder of the $4f_{7/2}$ peak in Fig. 1(b). Similar splits and dispersions of the $4f$-derived bands near the $\overline{\Gamma}$ point were observed in the Yb $4f$ systems and were reproduced by the periodic Anderson model implementing the c-f hybridization [13,21,22]. Away from the $\overline{\Gamma}$ point (cuts #1 to #3), an electronlike band leaves the lower branch for the $\overline{M}$ point, as indicated by the arrows in Figs. 2(b1)–2(b3). Interestingly, the lower branch still exists at $k \simeq 0$ Å^{-1} in the spectra of cuts #2 and #3, indicating an overlap of the conduction bands at the high-symmetry $\overline{\Gamma}$ point.

As a guide for the momentum dependence of the $4f$ bands, we present the LDA band structure calculations obtained with open-core treatment. Figure 3(a) shows the element- and orbital-projected density of states over an energy range spanning 10 eV around the Fermi level. The large density of states at $1.8 \leqslant |\omega| \leqslant 4.2$ eV is formed by the Cu d states. The Cu s, p, and d and In s and p states cross E_F in our calculations. As indicated by an arrow in the inset of Fig. 3(a), the non-f density of states is suppressed near E_F. This low density of states (quasigap) is characteristic of YbXCu$_4$ compounds ($X = $ Ag, Cd, In, Sn, etc.) [45,46].

The LDA band structure of YbInCu$_4$ in Figs. 3(b) and 3(c) indicates that the conduction bands around E_F have primarily Cu s, p, and d characters with a small contribution from the In s and p states. Moreover, the hole- and electronlike bands cross E_F around the W and X points, respectively. We note that there is a saddle point below E_F of the L point; the band in the Γ-L line is holelike, with a top, and the one in the K-L line is electronlike, with a bottom, as indicated by the yellow circle in Fig. 3(b). A saddle-point-like structure is also located at the X point. Our calculation in Figs. 3(b) and 3(c) agrees well with that for the non-f reference compound LuInCu$_4$, which is a semimetal with a small carrier density [41].

In the LDA result in Figs. 3(d)–3(f), the f bands hybridize with the two conduction bands, and the hybridization gap in the Γ-W direction is larger than that in the W-X-Γ direction. This implies that the c-f hybridization is more effective in the holelike band around the W point than in the electronlike band around the X point. We have found that the upper branch around the Γ point is the nondispersive (flat) band, as highlighted by the yellow region in Fig. 3(e). In addition, the saddle point at the L point is present near E_F. These characteristic bands derived from the c-f hybridization produce a high density of states at E_F. This is consistent with the fact that the electronic structure switches from a semimetallic state
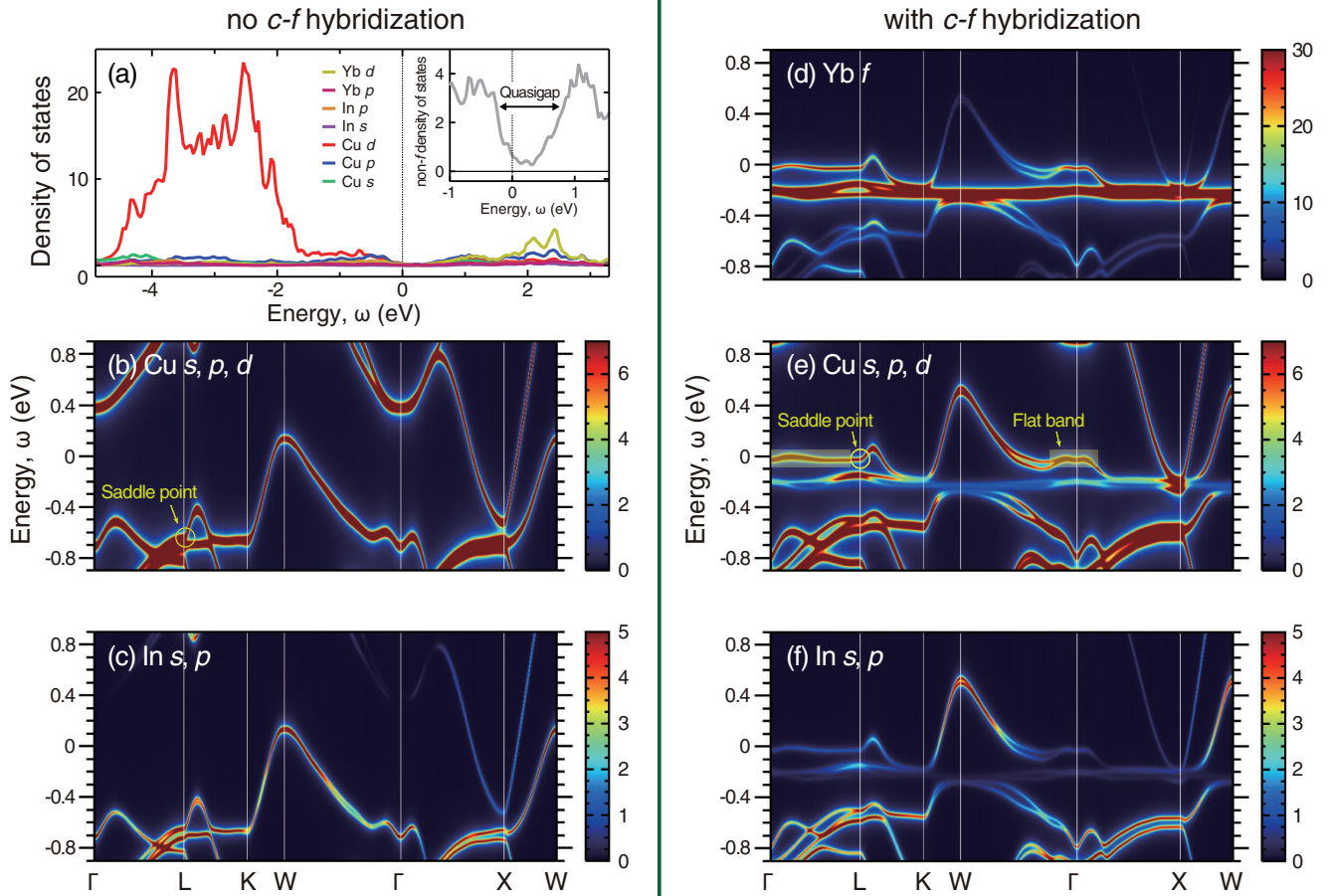
FIG. 3. LDA band structure of YbInCu$_4$ obtained with open-core treatment. (a) Element- and orbital-projected density of states. The inset represents an enlarged view of the non-f density of states, obtained by integrating the density of states of the conduction bands. The quasigap region is highlighted by the arrow. (b) and (c) The intensities for Cu s, p, and d and In s and p orbitals with no c-f hybridization, respectively. (d)–(f) The intensities for Yb f, Cu s, p, and d, and In s and p orbitals with c-f hybridization, respectively. Note that the intensities indicate the weights of the Bloch functions at each k point projected on the constituent orbitals (Wannier functions of Yb, Cu, and In). The flat band and saddle point are indicated by the yellow-colored region and yellow circles, respectively, in (b) and (e).

with $T_K \simeq 25$ K above T_V to a metallic state with $T_K \simeq 400$ K below T_V [5–8].

Hereafter, we focus on the band dispersion within an energy range of $E_F \leqslant |\omega| \leqslant 0.05$ eV. Figure 4(a) shows the Fermi surface map at $T = 10$ K in the low-temperature phase. The map is symmetrized by flipping and rotating the raw data along the high-symmetry lines. This procedure can reduce geometrical effects on the spectral intensity related to photoemission matrix elements and yields a clear view of the Fermi surface of YbInCu$_4$ [47]. The elliptical shape of the intensity contours is observed around the Brillouin zone corner. In Figs. 4(b1)–4(b3), we show the ARPES spectra along three momentum directions (cut 1 to cut 3), which are indicated by green curves in Fig. 4(a). The $4f_{7/2}$ states are observed as bright regions at $|\omega| \simeq 0.04$ eV. A small, but finite, weight of the conduction band exists at $|\omega| \leqslant 0.03$ eV. This band reaches E_F and can be assigned to the electron band, as demonstrated by the peak positions of the momentum distribution curves (MDCs) in Figs. 4(b1)–4(b3) and 4(c). The presence of the electron band on approaching E_F is also evident in the second-derivative ARPES images with respect to momentum, as discussed in the Appendix.

We determined the Fermi momentum k_F from the peak positions of the MDCs at E_F and plot them using open circles in Fig. 4(a) and white arrows in Figs. 4(b1)–4(b3). The electron band forms the elliptical Fermi pocket centered at the $\overline{M}$ point. This is consistent with our calculation in Figs. 3(d)–3(f), taking into consideration the surface Brillouin zone of the projected (111) plane. However, the results around the $\overline{\Gamma}$ point do not match our calculation, namely, a hole pocket near the L point. The reason for this discrepancy may be the insufficient experimental resolutions and the k_z dispersion of the electronic structure.

The ARPES data at $T = 50$ K in the high-temperature phase are shown in Figs. 4(d)–4(f). The elliptical electron Fermi surface still exists around the $\overline{M}$ point, as shown in Fig. 4(d). It should be noted that the Fermi momentum of the electron band shifts toward $k = 0$ Å^{-1}, causing a shrinkage of the Fermi surface above T_V. The peak positions of the MDCs at both $T = 10$ and 50 K in cut 3 are summarized in Fig. 4(g), revealing a rigid-band-like behavior of the electron band at T_V.

For a quantitative analysis, the MDC peak positions in the momentum direction of cut 3 are fitted by a quadratic dispersion of $a + b\omega^2$, and the results are plotted as dashed curves
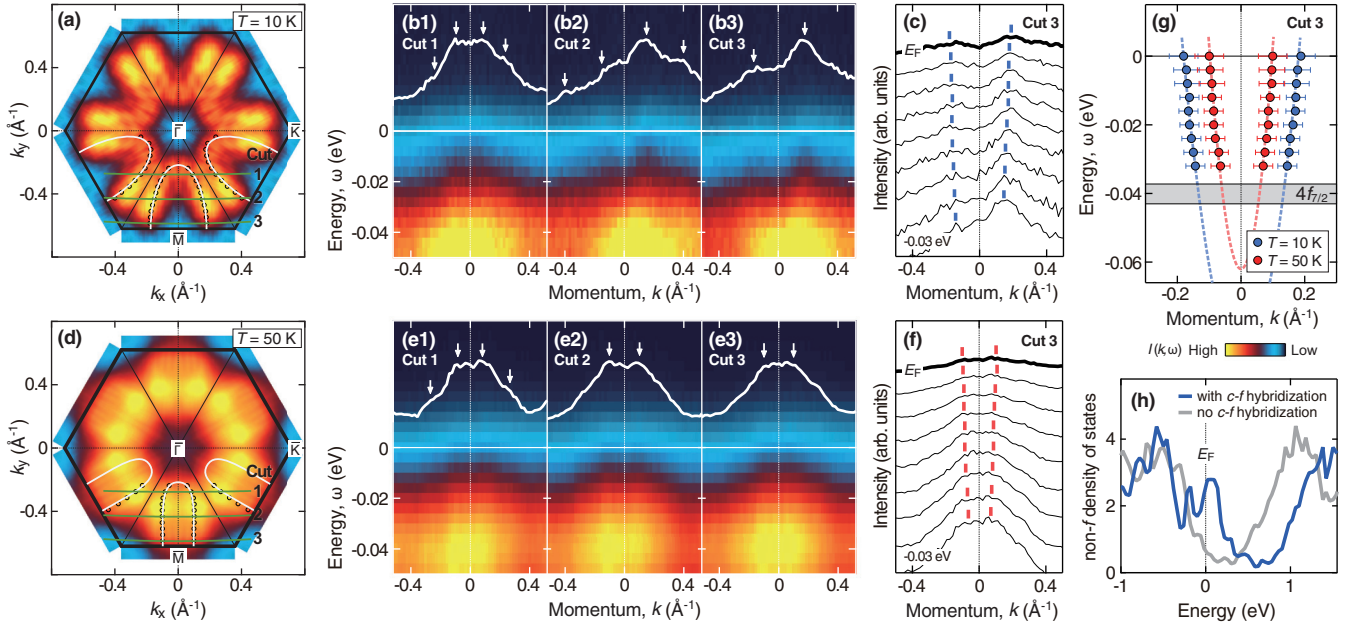
FIG. 4. Temperature-dependent Fermi surface evolution of YbInCu$_4$. (a) Fermi surface map at $T = 10$ K. The map is obtained by integrating the spectral intensity over an energy window of $|E_F| \leqslant 0.01$ eV and symmetrized by flipping and rotating the raw data along the high-symmetry lines. The thick black line indicates the boundary of the two-dimensional Brillouin zone. The black open circles represent the Fermi momentum k_F. The white outlines denote a Fermi surface constructed by tracking k_F. (b1)–(b3) Band dispersion at $T = 10$ K along three momentum cuts, as labeled in (a). The momentum distribution curves (MDCs) at E_F are also displayed as white curves. The white arrows indicate the peak positions of the MDCs. (c) MDCs of the ARPES spectra along cut 3 in (b3) in an energy range of $0 \leqslant |\omega| \leqslant 0.03$ eV. The blue vertical bars indicate the peak positions. (d) Fermi surface map at $T = 50$ K. The integration energy window, the lines, and the marks are the same as those in (a). (e1)–(e3) Band dispersion at $T = 50$ K along three momentum cuts, as labeled in (d). (f) MDCs of the ARPES spectra at $T = 50$ K along cut 3 in (e3). (g) Summary of the peak positions in (c) and (f). The blue and red circles are the peak positions of MDCs at $T = 10$ and 50 K, respectively. The dashed curves are quadratic dispersions of $a + b\omega^2$. The fitting parameters are set to $(a, b) = (-0.09, 2.7)$ and $(-0.06, 6.5)$ at $T = 10$ and 50 K, respectively. The gray shaded area represents the energy of the Yb^{2+} $4f_{7/2}$ states. (h) Comparison of the non-f density of states obtained by open-core LDA calculations. The blue and gray curves indicate the non-f density of states with c-f hybridization and without c-f hybridization, respectively. The result without c-f hybridization is the same data as in the inset of Fig. 3(a).

in Fig. 4(g). The parameters are set to $(a, b) = (-0.09, 2.7)$ and $(-0.06, 6.5)$ for the low- and high-temperature phases, respectively. The curvature of the band dispersion decreases below T_V along with the energy shift of 0.03 eV, implying a change in the strength of the hybridization between the $4f_{7/2}$ states and the conduction bands [22].

The ratio of the band velocities for the bare and renormalized electrons is an indicator of the correlation-induced enhancement of the effective mass [48–50]. We can extract a similar quantity, namely, the mass enhancement factor, from the ratio between the Fermi velocity in the high-temperature phase v_F^{HT}, which approximates the velocity with no c-f hybridization, and the hybridized Fermi velocity in the low-temperature phase v_F^{LT}. The two velocities are determined by differentiating the fitting data in Fig. 4(g) and are summarized in Table I together with their ratio. The mass enhancement factor of $v_F^{HT}/v_F^{LT} = 1.33 \pm 0.07$ provides direct evidence of the increase in the hybridization strength below T_V [22,46,51]. We note that errors come from the fit error and the statistical error in photoelectron counting.

Based on the identified band dispersion, we have estimated the area of the Fermi surface from Figs. 4(a) and 4(d). For a two-dimensional Fermi surface, the number of conduction electrons per unit cell n is given by the Luttinger theorem as

$n = A_{FS}/A_{BZ}$, where A_{FS} is the area of the Fermi surface and A_{BZ} is the area of the surface-projected Brillouin zone [52]. We found that the number n in the low- and high-temperature phases is $n_{LT} = 0.51$ and $n_{HT} = 0.33$ per surface unit cell of the YbInCu$_4$ (111) plane, respectively. The ratio of $n_{LT}/n_{HT} = 1.55 \pm 0.10$ demonstrates a reconstruction from a small to a large Fermi surface at T_V, where the error is mainly caused by the experimental uncertainty in determining the location of the k_F points. The enhancement of the carrier mobility at

TABLE I. Physical parameters of YbInCu$_4$ at $T = 10$ K in the low-temperature (LT) phase and at $T = 50$ K in the high-temperature (HT) phase. The Fermi velocity v_F was determined by differentiating the fitting result shown in Fig. 4(g). The electron number n was estimated using the Luttinger theorem, which indicates that the area of the two-dimensional Fermi surface is equal to the carrier density [52].

Phase	v_F (eVÅ)	v_F^{HT}/v_F^{LT}	n	n_{LT}/n_{HT}
LT	0.97		0.51	
HT	1.29	1.33	0.33	1.55

E_F is in good agreement with the substantial reduction in the electrical resistivity in the low-temperature phase [5–8].

Our observations on YbInCu$_4$ are consistently explained by the concept that the Kondo temperature and the Yb valence are associated with the position of the Fermi level relative to the quasigap [40–46]. The Yb valence drops from $z \simeq 2.90$ in the high-temperature phase to 2.72 in the low-temperature phase [5,6,38]. It is reasonable to consider that the electrons of the conduction band are transferred into Yb $4f$ states and then some Yb ions become divalent below T_V [40]. As shown by the rigid-band-like shift of the conduction band in Figs. 4(c), 4(f), and 4(g), this charge transfer results in the energy shift of the Yb $4f$ states and the non-$4f$ density of states toward the opposite side. Figure 4(h) shows the non-f density of states with c-f hybridization and without c-f hybridization obtained with the LDA calculations, revealing that the energy shift pushes the quasigap away from the Fermi level and consequently recovers a healthy density of states at E_F [45,46]. This situation enhances the hybridization strength below T_V, as demonstrated by $v_F^{HT}/v_F^{LT} = 1.33$ and $n_{LT}/n_{HT} = 1.55$. Therefore, two hybridization states, namely, a semimetallic state ($T > T_V$) with $T_K \sim 25$ K and a metallic state ($T < T_V$) with $T_K \sim 400$ K, are allowed in YbInCu$_4$ [8–10]. Our findings indicate that the enhancement in the density of states at E_F due to the c-f hybridization should be incorporated into scenarios of the first-order valence transition of YbInCu$_4$.

IV. CONCLUSION

In conclusion, we have presented a clear view of the electronic structure of YbInCu$_4$, including the hybridized bands and the Fermi surfaces, by using ARPES measurements and LDA calculations. We experimentally identified the elliptical Fermi surface pocket centered at the $\overline{M}$ point in the two-dimensional Brillouin zone. Below T_V, the area of the Fermi surface increases with an accompanying decrease in the Fermi velocity, demonstrating the crossover from a small to a large Fermi surface. These results confirm the development of the c-f hybridization in the low-temperature phase. The hybridization of the Yb f bands with the Cu s, p, and d and In s and p states forms a flat band around the Γ point. In addition, the VHS with the saddle point approaches the Fermi level. The presence of these characteristics in the band structure induces a high density of states at E_F and pushes the quasigap away from the Fermi level. Our results indicate that the c-f hybridization and the enhanced density of states at E_F play an important role in the emergence of the first-order valence transition of YbInCu$_4$.

Note added. Recently, we became aware of an article reporting the electronic band structure of YbInCu$_4$ [53]. There, the authors concluded that the band forms elliptical electron pockets in the Fermi surface around the $\overline{M}$ point, which is in agreement with our observations.

APPENDIX: SECOND-DERIVATIVE IMAGE METHOD

We here verify the fine feature of the conduction band near E_F. Figures 5(a)–5(c) show the second derivative of the photoemission intensity at $T = 10$ K with respect to the momentum $\partial^2 I(k, \omega)/\partial k^2$. This analysis method is often used to suppress undesirable backgrounds and sharpen the appearance of spectral features in ARPES images. By applying the method to the raw ARPES images of Figs. 4(b1)–4(b3), the nondispersive $4f_{7/2}$ band at $|\omega| \simeq 0.04$ eV is weakened, and the conduction band on approaching E_F is strengthened. The Fermi momenta k_F of the electron bands in Figs. 4(b1)–4(b3) are overlaid with white arrows, which coincide with the E_F crossing points of bands in Figs. 5(a)–5(c). This consistency demonstrates the reliability and accuracy of the data analysis.
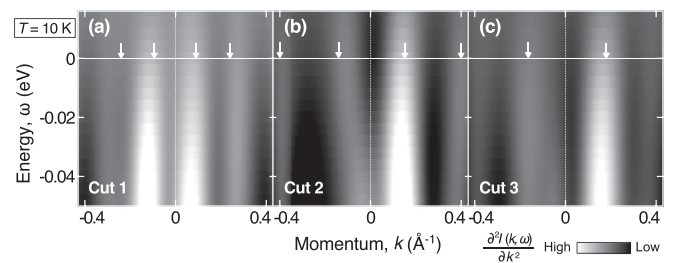

FIG. 5. (a)–(c) Second-derivative images of the ARPES spectra with respect to momentum $\partial^2 I(k, \omega)/\partial k^2$ for the data set in Figs. 4(b1)–4(b3). The momentum cuts are described by green lines in Fig. 4(a). The white arrows indicate the Fermi momenta of the electron bands shown in Figs. 4(b1)–4(b3).

[1] B. Johansson, Energy position of $4f$ levels in rare-earth metals, Phys. Rev. B **20**, 1315 (1979).

[2] C. M. Varma, Mixed-valence compounds, Rev. Mod. Phys. **48**, 219 (1976).

[3] S. Watanabe, A. Tsuruta, K. Miyake, and J. Flouquet, Valence fluctuations revealed by Magnetic field and pressure scans: Comparison with experiments in YbXCu$_4$ (X = In, Ag, Cd) and CeYIn$_5$ (Y = Ir, Rh), J. Phys. Soc. Jpn. **78**, 104706 (2009).

[4] S. Watanabe and K. Miyake, Quantum Valence Criticality as an Origin of Unconventional Critical Phenomena, Phys. Rev. Lett. **105**, 186403 (2010).

[5] I. Felner, I. Nowik, D. Vaknin, U. Potzel, J. Moser, G. M. Kalvius, G. Wortmann, G. Schmiester, G. Hilscher, E. Gratz, C. Schmitzer, N. Pillmayr, K. G. Prasad, H. de Waard, and H. Pinto, Ytterbium valence phase transition in Yb$_x$In$_{1-x}$Cu$_2$, Phys. Rev. B **35**, 6956 (1987).

[6] J. L. Sarrao, C. D. Immer, Z. Fisk, C. H. Booth, E. Figueroa, J. M. Lawrence, R. Modler, A. L. Cornelius, M. F. Hundley, G. H. Kwei, J. D. Thompson, and F. Bridges, Physical properties of YbXCu$_4$ (X = Ag, Au, Cd, Mg, Tl, and Zn) compounds, Phys. Rev. B **59**, 6855 (1999).

[7] B. Kindler, D. Finsterbusch, R. Graf, F. Ritter, W. Assmus, and B. Luthi, Mixed-valence transition in YbInCu$_4$, Phys. Rev. B **50**, 704 (1994).

[8] J. L. Sarrao, C. D. Immer, C. L. Benton, and Z. Fisk, Evolution from first-order valence transition to heavy-fermion behavior in YbIn$_{1-x}$Ag$_x$Cu$_4$, Phys. Rev. B **54**, 12207 (1996).

[9] T. Koyama, M. Matsumoto, T. Tanaka, H. Ishida, T. Mito, and S. Wada, Physical properties of the dense Kondo compounds YbXCu$_4$ (X = Au, Ag, In, Cd, Tl, and Mg) probed by ^{64}Cu NMR, Phys. Rev. B **66**, 014420 (2002).

[10] J. L. Sarrao, A. P. Ramirez, T. W. Darling, F. Freibert, A. Migliori, C. D. Immer, Z. Fisk, and Y. Uwatoko, Thermodynamics of the first-order valence transition in YbInCu$_4$, Phys. Rev. B **58**, 409 (1998).

[11] B. Cornut and B. Coqblin, Influence of the crystalline field on the Kondo effect of alloys and compounds with cerium impurities, Phys. Rev. B **5**, 4541 (1972).

[12] D. G. Koskenmaki and K. A. Gschneidner, Jr., in *Handbook on the Physics and Chemistry of Rare Earths*, edited by K. A. Gschneidner, Jr., and L. R. Eyring (North-Holland, Amsterdam, 1978), p. 337.

[13] S. Jang, J. D. Denlinger, J. W. Allen, V. S. Zapf, M. B. Maple, J. N. Kim, B. G. Jang, and J. H. Shim, Evolution of the Kondo lattice electronic structure above the transport coherence temperature, Proc. Natl. Acad. Sci. USA **117**, 23467 (2020).

[14] S. Ernst, S. Kirchner, C. Krellner, C. Geibel, G. Zwicknagl, F. Steglich, and S. Wirth, Emerging local Kondo screening and spatial coherence in the heavy-fermion metal YbRh$_2$Si$_2$, Nature (London) **474**, 362 (2011).

[15] H. Anzai, A. Ino, M. Arita, H. Namatame, M. Taniguchi, K. Fujita, M. Ishikado, S. Ishida, and S. Uchida, Relation between the nodal and antinodal gap and critical temperature in superconducting Bi2212, Nat. Commun. **4**, 1815 (2013).

[16] Y. Nakashima, A. Ino, S. Nagato, H. Anzai, H. Iwasawa, Y. Utsumi, H. Sato, M. Arita, H. Namatame, M. Taniguchi, T. Oguchi, Y. Aiura, I. Hase, K. Kihou, C. H. Lee, A. Iyo, and H. Eisaki, Fermi-surface reconstruction involving two Van Hove singularities across the antiferromagnetic transition in BaFe$_2$As$_2$, Solid State Commun. **157**, 16 (2013).

[17] A. C. Hewson, *The Kondo Problem to Heavy Fermions* (Cambridge University Press, Cambridge, 1993).

[18] A. N. Tahvildar-Zadeh, M. Jarrell, and J. K. Freericks, Low-Temperature Coherence in the Periodic Anderson Model: Predictions for Photoemission of Heavy Fermions, Phys. Rev. Lett. **80**, 5168 (1998).

[19] J. D. Denlinger, G.-H. Gweon, J. W. Allen, C. G. Olson, M. B. Maple, J. L. Sarrao, P. E. Armstrong, Z. Fisk, and H. Yamagami, Comparative study of the electronic structure of XRu$_2$Si$_2$: Probing the Anderson lattice, J. Electron Spectrosc. Relat. Phenom. **117**, 347 (2001).

[20] M. Güttler, K. Kummer, K. Kliemt, C. Krellner, S. Seiro, C. Geibel, C. Laubschat, Y. Kubo, Y. Sakurai, D. V. Vyalikh, and A. Koizumi, Visualizing the Kondo lattice crossover in YbRh$_2$Si$_2$ with Compton scattering, Phys. Rev. B **103**, 115126 (2021).

[21] S. Ishihara, K. Ichiki, K. Abe, T. Matsumoto, K. Mimura, H. Sato, M. Arita, E. F. Schwier, H. Iwasawa, K. Shimada, H. Namatame, M. Taniguchi, T. Zhuang, K. Hiraoka, and H. Anzai, The c-f hybridization effect in the subsurface region of YbInCu$_4$, J. Electron Spectrosc. Relat. Phenom. **220**, 66 (2017).

[22] H. Anzai, S. Ishihara, K. Mimura, H. Sato, M. Arita, T. Zhuang, and K. Hiraoka, Abrupt change in hybridization gap at the valence transition of YbInCu$_4$, Phys. Rev. Res. **2**, 033408 (2020).

[23] L. Van Hove, The occurrence of singularities in the elastic frequency distribution of a crystal, Phys. Rev. **89**, 1189 (1953).

[24] C. J. Halboth and W. Metzner, d-Wave Superconductivity and Pomeranchuk Instability in the Two-Dimensional Hubbard Model, Phys. Rev. Lett. **85**, 5162 (2000).

[25] K. Hiraoka, K. Murakami, S. Tomiyoshi, T. Hihara, T. Shinohara, and K. Kojima, ^{63}Cu NQR and ^{113}Cd NMR studies of YbMCu$_4$ (M = In, Cd), Phys. B **281–282**, 173 (2000).

[26] C. Moriyoshi, S. Shimomura, K. Itoh, K. Kojima, and K. Hiraoka, Crystal structure and valence transition temperature of YbInCu$_4$ single crystals, J. Magn. Magn. Mater. **260**, 206 (2003).

[27] P. Blaha, K. Schwarz, G. Madsen, D. Kvasnicka, and J. Luitz, *Wien2k: An Augmented Plane Wave + Local Orbitals Program for Calculating Crystal Properties* (Karlheinz Schwarz, Technische Universitat Wien, Vienna, 2001).

[28] J. P. Perdew and Y. Wang, Accurate and simple analytic representation of the electron-gas correlation energy, Phys. Rev. B **45**, 13244 (1992).

[29] O. Parcollet, M. Ferrero, T. Ayral, H. Hafermann, I. Krivenko, L. Messio, and P. Seth, TRIQS: A toolbox for research on interacting quantum system, Comput. Phys. Commun. **196**, 398 (2015).

[30] G. Kotliar, S. Y. Savrasov, K. Haule, V. S. Oudovenko, O. Parcollet, and C. A. Marianetti, Electronic Structure Calculations with Dynamical Mean-Field Theory, Rev. Mod. Phys. **78**, 865 (2006).

[31] M. C. Rahn *et al.*, Kondo quasiparticle dynamics observed by resonant inelastic x-ray scattering, Nat. Commun. **13**, 6129 (2022).

[32] H. Zhang, High-throughput design of magnetic materials, Electron. Struct. **3**, 033001 (2021).

[33] J. Kuneš, R. Arita, P. Wissgott, A. Toschi, H. Ikeda, and K. Held, Wien2wannier: From linearized augmented plane waves to maximally localized Wannier functions, Comput. Phys. Commun. **181**, 1888 (2010).

[34] A. A. Mostofi, J. R. Yates, G. Pizzi, Y.-S. Lee, I. Souza, D. Vanderbilt, and N. Marzari, An updated version of wannier90: A tool for obtaining maximally-localised Wannier functions, Comput. Phys. Commun. **185**, 2309 (2014).

[35] S. Tsutsui, K. Sugimoto, R. Tsunoda, Y. Hirose, T. Mito, R. Settai, and M. Mizumaki, First-order structural change accompanied by Yb valence transition in YbInCu$_4$, J. Phys. Soc. Jpn. **85**, 063602 (2016).

[36] *X-ray Data Booklet*, 3rd ed., edited by A. C. Thompson (Lawrence Berkeley National Laboratory, Berkeley, CA, 2009).

[37] F. Reinert, R. Claessen, G. Nicolay, D. Ehm, S. Hüfner, W. P. Ellis, G.-H. Gweon, J. W. Allen, B. Kindler, and W. Assmus, Photoemission experiments on YbInCu$_4$: Surface effects and temperature dependence, Phys. Rev. B **58**, 12808 (1998).

[38] H. Sato, K. Shimada, M. Arita, K. Hiraoka, K. Kojima, Y. Takeda, K. Yoshikawa, M. Sawada, M. Nakatake, H. Namatame, M. Taniguchi, Y. Takata, E. Ikenaga, S. Shin, K. Kobayashi, K. Tamasaku, Y. Nishino, D. Miwa, M. Yabashi, and T. Ishikawa, Valence Transition of YbInCu$_4$ Observed in Hard X-Ray Photoemission Spectra, Phys. Rev. Lett. **93**, 246404 (2004).

[39] S. Suga, A. Sekiyama, S. Imada, J. Yamaguchi, A. Shigemoto, A. Irizawa, K. Yoshimura, M. Yabashi, K. Tamasaku, A. Higashiya, and T. Ishikawa, Unraveling genuine first order bulk valence transition and Kondo resonance behaviors in YbInCu$_4$ by high energy photoelectron spectroscopy, J. Phys. Soc. Jpn. **78**, 074704 (2009).

[40] Y. Utsumi, H. Sato, H. Kurihara, H. Maso, K. Hiraoka, K. Kojima, K. Tobimatsu, T. Ohkochi, S. Fujimori, Y. Takeda, Y. Saitoh, K. Mimura, S. Ueda, Y. Yamashita, H. Yoshikawa, K. Kobayashi, T. Oguchi, K. Shimada, H. Namatame, and M. Taniguchi, Conduction-band electronic states of YbInCu$_4$ studied by photoemission and soft x-ray absorption spectroscopies, Phys. Rev. B **84**, 115143 (2011).

[41] V. N. Antonov, M. Galli, and F. Marabelli, Electronic structure and optical spectra of LuInCu$_4$ and YbMCu$_4$ ($M =$ Cu, Ag, Au, Pd, and In), Phys. Rev. B **62**, 1742 (2000).

[42] H. Anzai, S. Ishihara, H. Shiono, K. Morikawa, T. Iwazumi, H. Sato, T. Zhuang, K. T. Matsumoto, and K. Hiraoka, Mixed-valence state of the rare-earth compounds YbXCu$_4$ ($X =$ Mg, Cd, In, and Sn): Magnetic susceptibility, x-ray diffraction, and x-ray absorption spectroscopy investigations, Phys. Rev. B **100**, 245124 (2019).

[43] H. Anzai, K. Morikawa, H. Shiono, H. Sato, S.-I. Ideta, K. Tanaka, T. Zhuang, K. T. Matsumoto, and K. Hiraoka, Temperature dependence of Kondo resonance in photoemission spectra of the heavy-fermion compounds YbXCu$_4$ ($X =$ Mg, Cd, and Sn), Phys. Rev. B **101**, 235160 (2020).

[44] H. Anzai, R. Tawara, Y. Kikuchi, H. Sato, M. Arita, R. Takaaze, K. T. Matsumoto, and K. Hiraoka, Photoemission spectroscopy study on the heavy-fermion compound YbAgCu$_4$, J. Phys. Soc. Jpn. **91**, 114703 (2022).

[45] E. Figueroa, J. M. Lawrence, J. L. Sarrao, Z. Fisk, M. F. Hundley, and J. D. Thompson, Hall effect in YbXCu$_4$ and the role of carrier density in the YbInCu$_4$ valence transition, Solid State Commun. **106**, 347 (1998).

[46] I. Jarrige, A. Kotani, H. Yamaoka, N. Tsujii, K. Ishii, M. Upton, D. Casa, J. Kim, T. Gog, and J. N. Hancock, Kondo Interactions from Band Reconstruction in YbInCu$_4$, Phys. Rev. Lett. **114**, 126401 (2015).

[47] R. Kurleto, M. Fidrysiak, L. Nicolaï, J. Minár, M. Rosmus, L. Walczak, A. Tejeda, J. E. Rault, F. Bertran, A. P. Kądzielawa, D. Legut, D. Gnida, D. Kaczorowski, K. Kissner, F. Reinert, J. Spałek, and P. Starowicz, Photoemission signature of momentum-dependent hybridization in CeCoIn$_5$, Phys. Rev. B **104**, 125104 (2021).

[48] H. Anzai, A. Ino, T. Kamo, T. Fujita, M. Arita, H. Namatame, M. Taniguchi, A. Fujimori, Z.-X. Shen, M. Ishikado, and S. Uchida, Energy-Dependent Enhancement of the Electron-Coupling Spectrum of the Underdoped Bi$_2$Sr$_2$CaCu$_2$O$_{8+\delta}$ Superconductor, Phys. Rev. Lett. **105**, 227002 (2010).

[49] H. Anzai, M. Arita, H. Namatame, M. Taniguchi, M. Ishikado, K. Fujita, S. Ishida, S. Uchida, and A. Ino, Rapid enhancement of nodal quasiparticle mass with heavy underdoping in Bi2212, Phys. B (Amsterdam, Neth.) **536**, 667 (2018).

[50] M. Matsunami, T. Hajiri, H. Miyazaki, M. Kosaka, and S. Kimura, Strongly hybridized electronic structure of YbAl$_2$: An angle-resolved photoemission study, Phys. Rev. B **87**, 165141 (2013).

[51] M. Y. Zhang, R. Y. Chen, T. Dong, and N. L. Wang, Dramatic change of photoexcited quasiparticle relaxation dynamics across Yb valence state transition in YbInCu$_4$, Phys. Rev. B **95**, 165104 (2017).

[52] J. M. Luttinger, Fermi Surface and Some Simple Equilibrium Properties of a System of Interacting Fermions, Phys. Rev. **119**, 1153 (1960).

[53] H. Yang, J. Gao, Y. Cao, Y. Xu, A. Liang, X. Xu, Y. Chen, S. Liu, K. Huang, L. Xu, C. Wang, S. Cui, M. Wang, L. Yang, X. Luo, Y. Sun, Y.-F. Yang, Z. Liu, and Y. Chen, Observation of Mott instability at the valence transition of f-electron system, Natl. Sci. Rev. **10**, nwad03 (2023).